An Improved Model for the Heat-up Stage of the CAS-OB Process: Development and Validation

Aki Kärnä*, Mika Järvinen, Petri Sulasalmi,
Ville-Valtteri Visuri, Seppo Ollila and Timo Fabritius

A. Kärnä, P. Sulasalmi, V.-V. Visuri and Prof. T. Fabritius
Process Metallurgy Research Unit, University of Oulu, PO Box 4300, 90014 University of Oulu, Finland.
E-mail: aki.karna@oulu.fi
Prof. M. Järvinen
Department of Mechanical Engineering, Aalto University, PO Box 14440, 00076 Aalto, Finland.
S. Ollila
SSAB Europe Oy, Rautaruukintie 155, P.O.Box 93, 92101 Raahe, Finland
Keywords: CAS-OB, Chemical heating, Mathematical modeling,CFD

Details of chemical heating in the CAS-OB process are not known exactly, making a computational model is valuable in process development and control. A phenomena based numerical model of the CAS-OB heating stage is presented. Chemical equilibrium at reaction surfaces is assumed to be limited by mass transfer. Making use of a law of mass action based kinetic approach, reactions and mass transfer rates are solved simultaneously. Computational fluid dynamics was used to derive heat and mass transfer coefficients, which are then used in our model, consisting of only a few computational nodes. The model includes steel melt, slag and gas phases, bell and ladle structures, and three reaction fronts. Radiation, conduction and convection heat transfer are solved in the system. The model outputs temperatures and chemical composition of the system, and the results are validated with industrial data from two measurement campaigns.

1 Introduction

The CAS-OB process (Composition Adjustment by Sealed Argon Bubbling - Oxygen Blowing) is used to adjust steel composition and temperature before casting in steel production. The steel melt is heated by the reaction of aluminum and oxygen, which are fed simultaneously inside a snorkel into the melt surface. The closed space inside the bell ensures a slag-free melt surface and low-nitrogen atmosphere, making the reaction efficient. Typical heating rate is about 10°C per minute, and with intense heating it is possible to keep the batch liquid for hours.[1] The

using of CAS-OB process has been reported to yield greater production rate, lower costs and improve steel quality[2]. Because the details of chemical heating in the CAS-OB process are not known exactly, a computational predicting model is valuable in process control and process development.

Some numerical models of fluid flows in the CAS-OB process have been published[3,4], as have some physical scale models[5,6], but no other reaction models than our previous model[7] have been published.

Accurate process model needs all major chemical reactions to be taken into account, not just oxidation of aluminum. Mass transfer rates have a great impact on reaction balance, for which reason a plain chemical equilibrium calculation is not sufficient. There are not many suitable models available for restricted chemical equilibrium and so we have developed our own model, which is based on assumption that the reactions advance toward chemical equilibrium, the rate is limited only by mass transfer. The assumption is justified for most high-temperature reactions present in metallurgical processes.

We presented a formulation of our first version of the model in a previous publication, and its successful use[7]. The aim of the current paper is to further develop our previous model and validate it with industrial measurements. Development of our method includes a more accurate reaction model, a separate cooling model for uplifted bell and new heat and mass transfer coefficients from CFD simulations. These were needed to be able to simulate the actual process accurately, including all process steps. Measurement data from steel plant is used to compare temperatures from steel, ladle and bell, as well as chemical composition of steel and slag.

2 Methods

The model is based on reaction calculation method by Järvinen et al.[8], where the reactions are limited by mass transfer. The model does not have much spatial resolution compared to CFD; it only uses five control volumes and three reaction fronts. The conservation equations are solved by the implicit Newton's method. The model is updated from the first version[7] in many ways, including (see **Figure 1** for locations):

1. Radiation heat transfer is applied to all surfaces.
2. New heat and mass transfer correlation is calculated for the oxygen lance.
3. Effects of different argon blowing rates to fluid flows are taken into account.
4. CFD simulations are conducted for convective heat transfer coefficients at ladle and bell surfaces.
5. Realization of chemical equilibrium at reaction surfaces is monitored.
6. More detailed description of the temperature dependence of thermochemical properties (specific heat capacity, reaction enthalpy and reaction entropy) is added.

7. Reaction system is updated.

8. A new module is constructed for the situation in which the bell is uplifted.

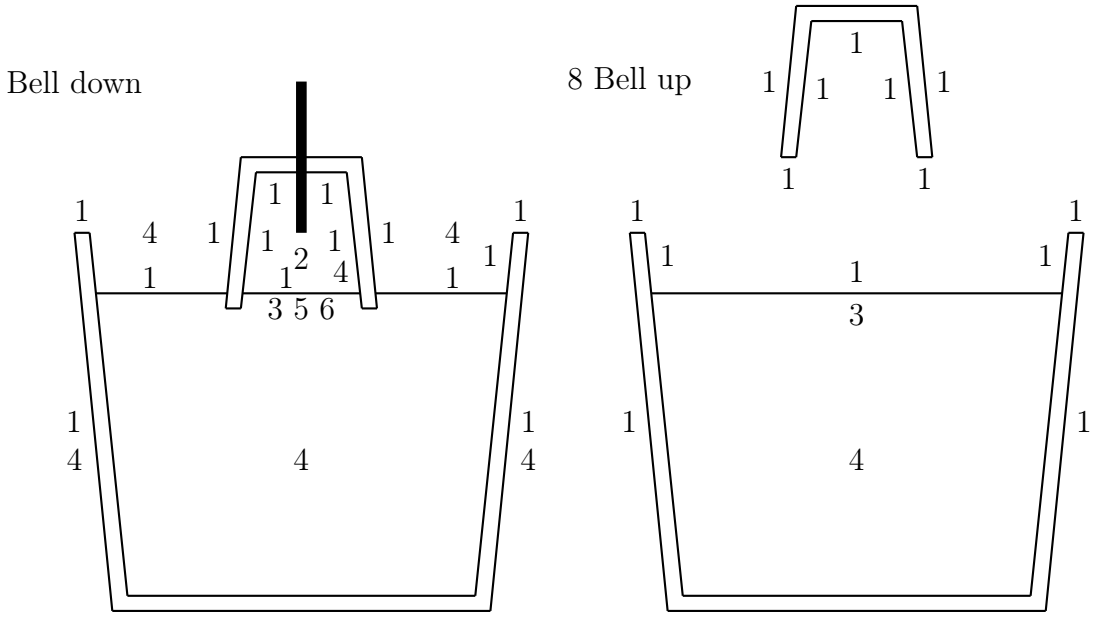

Figure 1. Modifications to the model.

The model involves two different geometries, which can be seen in **Figure 1**. During chemical heating, the bell is set at 0.3 m into melt, sealing the space inside the bell. After heating the bell is lift up above the ladle. The latter situation is included in the model in order to validate the model with bell cooling data. All reactions are assumed to take place inside the bell in the lowered position. The situation when oxygen is fed though supersonic lance blowing and aluminum particles are dropped inside the bell can be seen in **Figure 2**. The reactions take place at steel surface in the cavity, pure aluminum surface on top of slag layer and in the slag layer when jet-generated steel droplets fall back through it to melt.

2.1 CFD modeling for heat transfer coefficients

Since the reaction rates are limited by mass transfer, and since heat transfer is very important in a heating process, special attention is given to mass and heat transfer coefficients. Computational fluid dynamics (CFD) was used to define needed heat and mass transfer coefficients. Heat transfer was solved together with fluid flows by CFD providing the heat transfer coefficients. Mass transfer coefficients were then calculated using heat and mass transfer analogy. CFD models used in this work are summarized in **Table 1**. The role of the CFD modeling in this work is illustrated in **Figure 3**.

The CFD simulations were calculated using Ansys Fluent software with some user-defined function sub-routines. The determination of supersonic jet heat and mass transfer coefficients is explained in our previous publication[9]. The lance model was validated with experimental jet data found in literature. However, the heat transfer correlation is now calculated again by

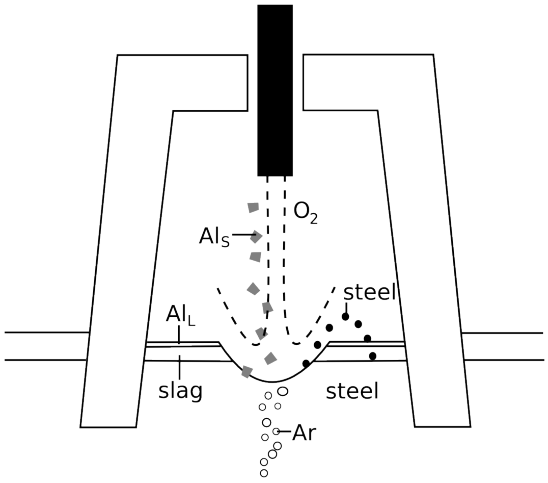

Figure 2. Bell, lance and phases during the heating stage.

Table 1. The CFD models used

CFD case	properties	results
Supersonic lance blowing[9]	Steady-state,axisymmetric 2D, compressible, modified k-ε	Lance heat transfer coefficient, bell interior heat transfer coefficient
External heat transfer	Steady-state, 3D, compressible, k-ε	Bell and ladle exterior heat transfer coefficients
Fluid flows in whole CAS-OB	Transient, 3D, incompressible, k-ε, Eulerian multiphase	Ladle interior heat transfed coefficient, melt surface mass transfer coefficient
View factors 1	3D, radiation only	View factors when bell down
View factors 2	3D, radiation only	View factors when bell up

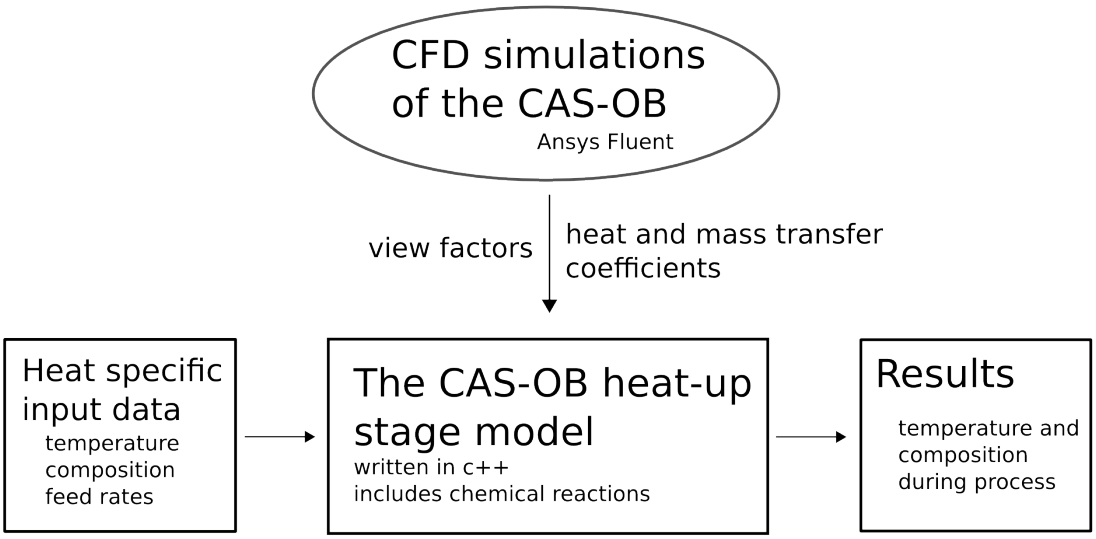

Figure 3. The role of CFD simulations.

considering heat transfer from bulk gas inside the bell to the melt surface. This is because in the process model, heat and mass transfer coefficients for lance blowing are used between the average value in the bell and the surface value. The old correlation was determined for heat transfer between lance and melt surface. The new correlation for lance blowing average heat transfer coefficient α_g is

$$\alpha_g = -115H_l + 453, \tag{1}$$

integrated over the whole melt surface inside the bell, where H_l is lance height from the melt surface. For more detailed reaction modeling, average heat and mass transfer coefficients are calculated separately for a free metal surface and for a pure aluminum surface in the reaction model, by integrating the radial heat transfer function h(r) obtained from CFD simulations.

$$\alpha_f = \frac{\int_0^{r_l} h(r) 2\pi r dr}{\int_0^{r_l} 2\pi r dr} \tag{2}$$

$$\alpha_{Al} = \frac{\int_{r_l}^{R} h(r) 2\pi r dr}{\int_{r_l}^{R} 2\pi r dr} \tag{3}$$

The same simulation setup was used to determine the convection heat transfer coefficient on the bell inside walls as a function of lance height.

$$\alpha_{bell,in} = -26H_l + 125 \tag{4}$$

A new CFD model was used to determine heat transfer coefficients outside the ladle and the bell. The model consists of only outside surfaces and an airspace. Energy boundary conditions were applied as constant temperatures at surfaces according to measurement data. Boundary condition for surrounding airspace was set at typical ambient temperature, still air. The convective flow of air induced by the surface heating was simulated, and average heat transfer

Table 2. Diffusion coefficients in steel melt, m/s^2 [15].

Al	C	Mn	Ni	Si	Fe
3.5×10^{-9}	1×10^{-8}	4.96×10^{-9}	4.83×10^{-9}	6×10^{-7}	4×10^{-9}

coefficient at the surface was calculated. Since heat radiation was not taken into account here, the coefficient is only for convective heat transfer and radiation can be applied separately in the process model. The average convective heat transfer coefficient for the outside surfaces was found to be 10 $W/(m^2K)$.

Another CFD model was used to calculate the heat transfer coefficient inside the ladle, from steel melt to ladle walls. The geometry involves the ladle interior and the bell (**Figure 4**). In this model, a small temperature difference was applied between the melt and ladle wall to find the heat transfer coefficient. Multiphase modeling was carried out as Eulerian two-phase flow with $k-\varepsilon$ turbulence model.Bubble size was set at constant 0.01 m according to experimental [10] and modeling [11] results. The argon bottom blowing rate was 500 l/min. The gas was modeled as being incompressible, therefore lance blowing was applied as a boundary condition 1 m down from the lance head, where the flow is no more supersonic and gas density is fairly close to ambient gas density. The supersonic flow solution was obtained from separate detailed simulations [9], which are modelled with compressible gas formulation. The average convective heat transfer coefficient for inner surface of the ladle was found to be 5450 $W/(m^2K)$ and 4100 $W/(m^2K)$ for submerged part of the bell. Lance blowing was found to have only minor effect on the heat transfer rate, bottom bubbling is the main source of melt movements.

In the steel melt surface mass transfer coefficient is given by correlation proposed by Kataoka et al. [12]

$$h_i = c \left(\frac{\varepsilon}{\nu}\right)^{\frac{1}{4}} D_i^{\frac{1}{2}}. \tag{5}$$

ε_i is turbulence dissipation rate taken from CFD model, D_i is diffusion coefficient for species i and ν kinematic viscosity of steel. In original work constant C was 0.5 for open channel flows, in bubbly flows constant C has been used with values 0.3 [13] and 0.5 [14]. In this work 0.3 is used. Diffusion coefficients are given in **Table 2**.

Heat and mass transfer analogy is used to obtain transfer coefficients in cases when only other coefficient is known [16]

$$\frac{Sh}{Sc^n} = \frac{Nu}{Pr^n}, \tag{6}$$

where n is 1/3 in this work. Mass transfer coefficient for each species i is given by

$$h_i = \frac{\alpha D_i}{k} \left(\frac{k}{\rho D_i c_p}\right)^n, \tag{7}$$

where k is heat conductivity and c_p is specific heat. The heat transfer coefficient is

$$\alpha = \frac{hk}{\left(\frac{k}{\rho D c_p}\right)^n}. \tag{8}$$

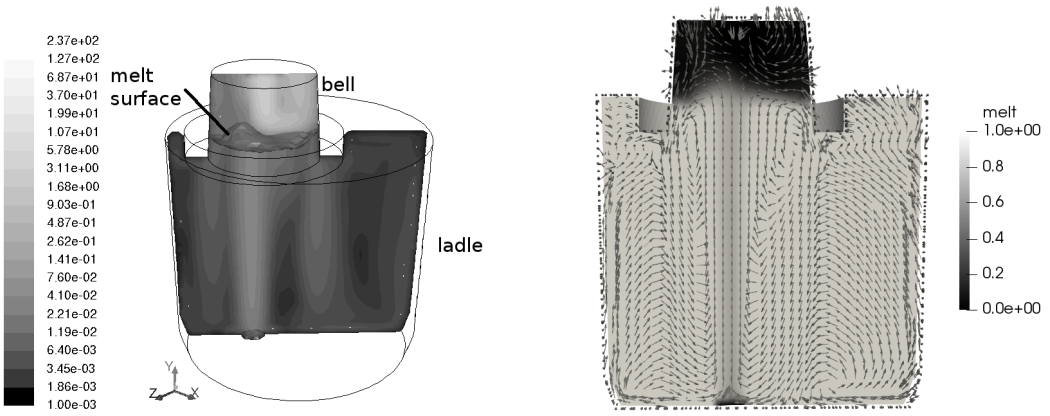

Figure 4. Whole CAS-OB CFD simulation, showing velocity on logarithmic scale and melt volume fraction with flow direction.

2.2 Modeling flow characteristics

Argon rising velocity is calculated by using the correlation proposed by Ebneth and Pluschkell [17] in order to account for different bottom bubbling rates. Open eye model for surface slag is needed for phases when the bell is elevated. The slag opening size is calculated by a correlation for dimensionless open eye from Krishnapisharody et al [18].

Heat transfer coefficient in the slag layer is estimated by an assumption that melt movement causes circulation in the slag layer. Shear stress in steel side of the phase boundary is

$$\tau = 0.5 c_f \rho_m (u_m - u_s)^2, \tag{9}$$

where $c_f = 0.0592 Re^{-1.5}$ is skin friction coefficient [16], u_m is average steel velocity below slag layer, estimated from argon rising velocity, the open eye size and slag layer area as $u_m = u_0 A_e / A_{slag}$. By assuming that the center of circulation is in the middle of the slag layer, the shear stress in slag is

$$\tau = \mu_s \frac{2u_s}{h_s}. \tag{10}$$

Slag velocity can be solved as

$$u_s = -\frac{-c_f h_s \rho_m u_m + 2(c_f h_s \mu_s \rho_m u_m + \mu_s^2)^{0.5} - 2\mu_s}{c_f h_s \rho_m} \tag{11}$$

and heat transfer coefficient is then estimated based on penetration model proposed by Higbie [19]

$$\alpha = 2\sqrt{\frac{k_s c_{p,s} \rho_s}{\pi L_s / u_s}}. \tag{12}$$

Depression on melt surface caused by oxygen jet from the lance is described by correlations by Koria and Lange [20]. The dimensionless momentum flux from lance $\underline{\dot{M}}$ is calculated as

$$\underline{\dot{M}} = \frac{\dot{V}_g \rho u_J}{\rho_l g H^3}, \tag{13}$$

where volume flux $\dot{V}_g$ and density ρ are in NTP conditions. Jet velocity u_J=475 m/s is obtained from CFD simulations[9]. H is the lance height, typically 1.5 m. The diameter d_f and depth h_f of the depression caused by the lance jet are

$$d_f = 2.813 H \underline{\dot{M}}^{0.282} \tag{14}$$

and

$$h_f = 4.469 H \underline{\dot{M}}^{0.66}. \tag{15}$$

The surface area of the depression, A_f, is calculated assuming spherical cap geometry

$$A_f = \pi \left(\frac{{d_f}^2}{2} + h_f^2 \right). \tag{16}$$

Solid aluminum particles are fed inside the bell through the bell top, the particles are assumed to melt and dissolve simultaneously in the melt. The remaining liquid aluminum is blown to the sides outside the free metal surface of the depression and oxidized there. Aluminum melting time is[7]

$$\tau_m = \frac{d_{Al}^2}{8} \frac{\rho_{Al} l_m}{\lambda_e \left(T_l - T_{m,Al} \right)}, \tag{17}$$

where λ_e is effectice conductivity, $T_{m,Al}$ is aluminum melting temperature, 933 K, l_m is the melting heat and T_l is melt temperature. The average melting rate of aluminum particles is estimated to be $1/\tau_m$ which is used in conservation equations.

Melt surface area inside the bell is divided to two areas: the free surface area of the depression A_f, and the occupied surface area A_O, where all slag and liquid aluminum are assumed to move by lance blowing. The slag layer is assumed to have the uniform thickness

$$h_s = \frac{m_s}{\rho_s S_O}. \tag{18}$$

The aluminum is assumed to float on top of slag layer, and the minimum thickness of the layer is set at 0.1 mm If there is less aluminum, the layer is smaller in area.

$$A_{Al} = min \left(A_{slag}, \frac{m_{Al}}{\rho_{Al} 0.0001 m} \right) \tag{19}$$

Steel droplet generation by lance jet is described by the model developed by Rout et al.[21], which adds the influence of a high-temperature environment to the model of Subagyo et al.[22]. Blowing number, which determines splashing rate is

$$N_B = \frac{\eta^2 \rho_g u_j^2}{2\sqrt{\rho_l \sigma_l g}}, \tag{20}$$

where the gas properties are at ambient temperature inside the bell. u_j is axial velocity of the gas jet, and η is a parameter with the value 0.4471, ρ_g and ρ_l are densities of gas and melt, σ_l is surface tension and g is gravitational acceleration. The droplet generation rate R_B is given by

$$R_B = \frac{F_g N_B^{3.2}}{(2.6 * 10^6 + 2.0 * 10^{-4} N_B^{12})^{0.2}}, \tag{21}$$

where F_g is volumetric gas flow rate calculated with correct density in high temperature. Mass of the droplets falling through the slag layer is calculated as $m_D = min(\tau_D, t)R_B$, where $\tau_D = \frac{h_s}{u_D}$. Droplet falling velocity u_D is calculated from terminal velocity assumption [23]

$$u_D = 0.153 \left(\frac{d_D g \left(\rho_M - \rho_s\right)}{\rho_s} \left(\frac{d_D \rho_s}{\mu_s} \right)^{0.6} \right)^{1/1.4}, \tag{22}$$

where d_D is droplet diameter. Mass transfer inside steel droplets falling through the slag layer is modelled with

$$h_{D,i} = 2\sqrt{\frac{D_{L,i}}{\pi d_D / u_D}}. \tag{23}$$

The mass m_D is used to calculate surface area of steel droplets in the slag.

$$A_d = \frac{6 m_D}{d_D \rho_l} \tag{24}$$

2.3 Reaction system

The following reactions in the melt surface are considered:

$$2\mathrm{Al(L)} + \tfrac{3}{2}\mathrm{O_2(g)} \rightleftarrows \mathrm{Al_2O_3(s)} \quad (r_1)$$
$$2\mathrm{Al(m)} + \tfrac{3}{2}\mathrm{O_2(g)} \rightleftarrows \mathrm{Al_2O_3(s)} \quad (r_2)$$
$$\mathrm{Si(m)} + \mathrm{O_2(g)} \rightleftarrows \mathrm{SiO_2(s)} \quad (r_3)$$
$$\mathrm{Mn(m)} + \tfrac{1}{2}\mathrm{O_2(g)} \rightleftarrows \mathrm{MnO(s)} \quad (r_4)$$
$$\mathrm{Fe(m)} + \tfrac{1}{2}\mathrm{O_2(g)} \rightleftarrows \mathrm{FeO(s)} \quad (r_5)$$
$$\mathrm{C(m)} + \tfrac{1}{2}\mathrm{O_2(g)} \rightleftarrows \mathrm{CO(g)} \quad (r_6)$$

The reaction in the gas phase:

$$\mathrm{CO(g)} + \tfrac{1}{2}\mathrm{O_2(g)} \rightleftarrows \mathrm{CO_2(g)} \quad (r_7)$$

The reactions between the steel droplets and the slag:

$$\mathrm{FeO(s)} + \tfrac{3}{2}\mathrm{Al(m)} \rightleftarrows \mathrm{Fe(m)} + \tfrac{1}{3}\mathrm{Al_2O_3(s)} \quad (r_8)$$
$$\mathrm{FeO(s)} + \tfrac{1}{2}\mathrm{Si(m)} \rightleftarrows \mathrm{Fe(m)} + \tfrac{1}{2}\mathrm{SiO_2(s)} \quad (r_9)$$
$$\mathrm{FeO(s)} + \mathrm{Mn(m)} \rightleftarrows \mathrm{Fe(m)} + \mathrm{MnO(s)} \quad (r_{10})$$

Phases are liquid aluminum (L), slag (s), steel melt (m) and gas (g).
Reaction rates are modelled by the law of mass action method developed by Järvinen et al. [8], where reactions are assumed to be limited by mass transfer rate. For example, the reaction rate for oxidation of dissolved aluminum in steel is

$$R = k_f \left(a_{Al}^2 a_{O_2}^{1.5} - \frac{a_{Al_2O_3}}{K} \right), k_f \to \infty, \tag{25}$$

where a_i is the activity for species i. Forward reaction rate constant k_f is set at sufficiently large but finite number in computation, this ensures that reaction rate is not the limiting factor but mass transfer is.

The equilibrium coefficients K_i are calculated from

$$K_i = exp\left(-\Delta G0_i/RT\right), \tag{26}$$

where $\Delta G0_i$ is Gibbs energy difference between products and reactants. Gibbs energy of each species is calculated as a function of temperature

$$G(T) = \Delta H_{T_0} + \int_{T_0}^{T} C_p(T)dT - T\left(S_{T_0} + \int_{T_0}^{T} \frac{C_p(T)}{T}dT\right). \tag{27}$$

Following formulas of heat capacity are used, for NIST database[24] coefficients and HSC database[25] coefficients, respectively.

$$C_p(T) = A + BT + CT^2 + DT^3 + \frac{E}{T^2} \tag{28}$$

$$C_p(T) = A + BT + CT^{-2} + DT^2 \tag{29}$$

A,B,C,D and E are database specific coefficients.

Activities of the species are calculated using Unified Interaction Parameter formalism (UIP) for metal components and quadratic formalism by Ban-Ya for slag components. The ideal gas law is used for gas phase activities.

UIP model activity coefficient γ_i for species i is defined as

$$ln\gamma_i = ln\gamma_i^0 + ln\gamma_{solvent} + \sum_{j=1}^{N} \epsilon_{ij} X_J, \tag{30}$$

γ_0 is interaction coefficient at infinite dilution, ϵ_{ij} is interaction coefficient and X_j is mole fraction. The activity coefficient of the solvent is given by

$$ln\gamma_{solvent} = -\frac{1}{2}\sum_{j=1}^{N}\sum_{k=1}^{N} \epsilon_{jk} X_J X_k. \tag{31}$$

The activity for the slag component i is given by Ban-Ya's formulation

$$RTln\gamma_i = \sum_{j=1}^{N} \alpha_{ij} X_j^2 + \sum_{j=1}^{N}\sum_{k=1}^{N} \left(\alpha_{ij} + \alpha_{ik} + \alpha_{jk}\right) X_J X_k + \Delta G_c, \tag{32}$$

where ΔG_c is the conversion factor between hypothetical regular solution and real solution. All interaction coefficients used are presented in previous paper[7].

The assumption of local chemical equilibrium at the reaction surface is verified during the calculation by comparing the reaction quotient to the equilibrium constant. The iterations are continued at each step time until K/Q equals unity with a low tolerance.[26] Q is the reaction quotient

$$Q = \frac{\prod_i a_i^{\nu_i}}{\prod_j a_j^{\nu_j}}, \tag{33}$$

where i denotes products, j reactants and ν is the stoichiometric coefficient.
In practice the forward reaction coefficient k_f needs to be a relatively big number, up to 10^{30}. This can cause numerical instability in computation, and therefore the coefficient is first set at a low value and then increased during computation of each timestep to keep the system stable. Pure aluminum phase causes challenges, because there is no limiting mass transfer inside a phase of pure reactant. In reaction 1, oxidation of Al by oxygen jet, the forward reaction coefficient is limited to 10^{20} for computational stability. This is not enough for chemical equilibrium, but at this reaction surface there are no competing reactions, and so the rate limiting mass transfer rate of oxygen is about $h_m(1.0 - 10^{-10})$ instead of $h_m(1.0 - x)$ where $x < 10^{-10}$. This makes the error caused by this limitation less than $10^{-8}\%$. Otherwise the calculation procedure is the same as in other reactions, except the K/Q criterion is not meaningful and not monitored.
The reactions between pure aluminum and slag are modelled through reactions 7-10, it is assumed that steel droplets mix with pure aluminum and then fall through slag layer. The exact mixing rate is quite impossible to know exactly and that includes an adjustable parameter.
Reactions take place at five different surfaces: steel-gas, steel-slag, steel droplet-slag, pure aluminum-gas and pure aluminum-slag. Mass fractions of species are calculated at seven points, bulk liquid steel, bulk gas, bulk slag, liquid-gas surface, liquid-slag surface, pure aluminum surface and steel droplet surface.

2.4 The mass conservation equations

There are 34 variables in the mass conservation system, which consist of 34 conservation equations. The conservation equations at reaction surfaces have no storage term, since the surface is assumed to be massless. Basic form of the species conservation equations at the reaction surfaces is

$$h\rho\frac{dy}{dx} + \dot{m}y = \sum \nu R_{surface}, \tag{34}$$

where $\dot{m}$ is total mass flow caused by all reactions. The bulk phases include the storage term

$$h\rho\frac{dy}{dx} + \dot{m}y = \sum \nu R_{bulk} - V\rho\frac{dy}{dt}. \tag{35}$$

The derivatives are discretized by using first-order approximations. The implicit Euler method is used in time integration.
Oxygen conservation equation at the free melt surface created by the gas jet is

$$h_{g,f}\rho_g\left(y_{O_2} - y_{O_2 f}\right) + max(\dot{m}_g, 0)y_{O_2} - max(-\dot{m}_g, 0)y_{O_2 f} = -\sum_{i=2}^{6} \nu_{i,O_2} R_i, \tag{36}$$

where $h_{g,f}$ is gas mass transfer coefficient including lance blowing for free melt surface, y_{O_2} is oxygen mass fraction in bulk gas, $y_{O_2 f}$ is gaseous oxygen mass fraction at free surface, $\dot{m}_g$ is

total gas flux including effect of all reactions and $\nu_{O_2,i}$ is mass based stoichiometric coefficient of oxygen in reaction i.
Oxygen at the pure aluminum surface surrounding the free surface area is conserved as

$$h_{g,Al}\rho_{g,Al}(y_{O_2} - y_{O_2,Al}) + max(\dot{m}_{g,Al}, 0)y_{O_2} - max(-\dot{m}_{g,Al}, 0)y_{O_2,Al} = -R_1\nu_{1,O_2}, \tag{37}$$

where $y_{O_2,Al}$ is oxygen mass fraction at pure aluminium surface. Oxygen conservation in bulk gas phase is

$$\begin{aligned}\dot{m}_{O_2,in} - \dot{m}_{g,out}y_{O_2} + R_7V_g\nu_{7,CO} \\ - h_{g,f}A_f\rho_{g,f}(y_{O_2} - y_{O_2,f}) - max(\dot{m}_g, 0)A_f y_{O_2} \\ + max(-\dot{m}_g, 0)A_f y_{O_2,f} - h_{g,Al}A_{Al}\rho_{g,Al}(y_{O_2} - y_{O_2,Al}) \\ - max(\dot{m}_{g,0}, 0)A_{Al}y_{O_2} + max(-\dot{m}_{g,0}, 0)A_{Al}y_{O_2,Al} = V_g\frac{d(\rho_g y_{O_2})}{dt}.\end{aligned} \tag{38}$$

$\dot{m}_{O_2,in}$ is mass flux of oxygen from the lance, $\dot{m}_{g,out}$ is the total mass flux of gas leaving the bell, $h_{g,Al}$ is oxygen mas transfer coefficient for aluminum layer around the free surface, A_f and A_{Al} are surface areas of the free surface and aluminum surface, respectively. Gas density is different at the surfaces, since the temperature is not the same.
Carbon monoxide conservation in bulk gas includes reaction with oxygen and carbon dioxide

$$\begin{aligned}- \dot{m}_{g,out}y_{CO} - h_{CO,f}A_f\rho_{g,f}(y_{CO} - y_{CO,f}) - max(\dot{m}_g, 0)A_f y_{CO} \\ + max(-\dot{m}_g, 0)A_f y_{CO,f} + R_7V_g\nu_{7,CO} = V_g\frac{d(\rho_g y_{CO})}{dt}.\end{aligned} \tag{39}$$

Carbon monoxide at the reaction surface is conserved as

$$h_{CO}\rho_{g,f}(y_{CO} - y_{CO,f}) + max(\dot{m}_g, 0.0)y_{CO} - max(-\dot{m}_g, 0.0)y_{CO,f} = -R_6\nu_{6,CO}. \tag{40}$$

Carbon dioxide conservation in bulk gas volume and in reaction surface are respectively:

$$\begin{aligned}- \dot{m}_{g,out}y_{CO_2} - h_{CO_2}A_f\rho_{g,f}(y_{CO_2} - y_{CO_2,f}) \\ + max(\dot{m}_g, 0.0)y_{CO_2} - max(-\dot{m}_g, 0.0)y_{CO_2,f} + R_7V_g\nu_{7,CO_2} = V_g\frac{d(\rho_g y_{CO_2})}{dt}\end{aligned} \tag{41}$$

$$h_{CO_2}\rho_{g,f}(y_{CO_2} - y_{CO_2,f}) + max(\dot{m}_g, 0.0)y_{CO_2} - max(-\dot{m}_g, 0.0)y_{CO_2,f} = 0 \tag{42}$$

Argon is given by gas phase sum equations, for bulk gas

$$y_{O_2,f} + y_{CO,f} + y_{CO_2,f} + y_{Ar,f} = 1.0 \tag{43}$$

and for surface

$$y_{O_2} + y_{CO} + y_{CO_2} + y_{Ar} = 1.0. \tag{44}$$

Mass of solid aluminum $m_{Al,S}$ inside the bell is determined by aluminum feed rate $\dot{m}_{Al,s}$ and melting rate R_{melt} ,

$$\dot{m}_{Al,S} - m_{Al,S}R_{melt} = \frac{dm_{Al,S}}{dt}. \tag{45}$$

Liquid pure aluminum involves also dissolving into bulk melt directly and via melt droplets falling through liquid Al layer. The conservation equation for liquid aluminum phase is

$$m_{Al,S}R_{melt} + h_{Al,L}A_d(y_{Al,d} - 1.0) + h_{Al,S}A_{Al,S}\rho_l(y_{Al} - 1.0) + \nu_{1,Al}A_{Al}R_1 = \frac{dm_{Al_l}}{dt}. \tag{46}$$

$h_{Al,L}$ is the mass transfer coefficient of aluminum into steel droplets, A_d is steel droplet surface area in liquid aluminum, $h_{Al,S}$ is mass transfer coefficient for solid aluminum particles in steel and $A_{Al,S}$ is the surface area of the aluminiun particles in contact with steel $A_{Al,S} = 0.42m_{Al_S}6/\left(\rho_{Al_S}d_{Al}\right)$. The factor 0.42 is the fraction of the surface that is touching the steel melt when particles float on the surface.
Conservation equation for aluminum in bulk steel melt is

$$\begin{aligned} &- h_{Al}A_f\rho_l(y_{Al} - y_{Al,f}) - max(\dot{m}_l, 0.0)A_f y_{Al} \\ &\quad + max(-\dot{m}_l, 0.0)A_f y_{Al,f} - h_{Al,d}A_d\rho_l(y_{Al} - y_{Al,d}) \\ &\quad - max(\dot{m}_{L,d}, 0.0)A_d y_{Al} + max(-\dot{m}_{L,d}, 0.0)A_d y_{Al,d} \\ &\quad - h_{Al,S}A_{Al,S}\rho_l(y_{Al} - 1.0) = \frac{d(m_l y_{Al})}{dt}, \end{aligned} \tag{47}$$

and aluminum conservation at melt surface

$$A_f h_{Al}\rho_l(y_{Al} - y_{Al,f}) + A_f max(\dot{m}_l, 0.0)y_{Al} - A_f max(-\dot{m}_l, 0.0)A_f y_{Al,f} = -A_f R_2\nu_{2,Al}. \tag{48}$$

Aluminum conservation equation in steel droplets includes aluminum dissolution as droplets fall through the aluminum layer.

$$\begin{aligned} &h_{Al,L}A_d(1.0 - y_{Al,d}) + h_{Al,d}\rho_l(y_{Al} - y_{Al,d}) + max(\dot{m}_{L,d}, 0)y_{Al} \\ &\quad - max(-\dot{m}_{L,d}, 0)y_{Al,ds} = -R_8\nu_{8,Al} \end{aligned} \tag{49}$$

Conservation equations of other species in metal, Si,C,Mn,Ni and Fe are similar to each other and only Si is given as an example here. The conservation equation for silicon in steel melt is

$$\begin{aligned} &- h_{Si}A_f\rho_l(y_{Si} - y_{Si,f}) - max(\dot{m}_l, 0.0)A_f y_{Si} \\ &\quad + max(-\dot{m}_l, 0.0)A_f y_{Si,f} - h_{Si,d}A_d\rho_l(y_{Si} - y_{Si,d}) \\ &\quad - max(\dot{m}_{L,d}, 0.0)A_d y_{Si} + max(-\dot{m}_{L,d}, 0.0)A_d y_{Si,d} = \frac{d(m y_{Si})}{dt} \end{aligned} \tag{50}$$

and silicon at free melt surface is conserved as

$$h_{Si}\rho_l(y_{Si} - y_{Si,f}) + max(\dot{m}_l, 0.0)y_{Si} - max(-\dot{m}_l, 0.0)y_{Si,f} = -R_3\nu_{3,Si}. \tag{51}$$

Steel droplet surface silicon conservation is

$$h_{Si,d}\rho_l(y_{Si} - y_{Si,d}) + max(\dot{m}_{L,d}, 0.0)y_{Si} - max(-\dot{m}_{L,d}, 0.0)y_{Si,d} = -R_9\nu_{9,Si}. \tag{52}$$

Species in steel droplets are modelled using the assumption that reactions do not have time to affect the bulk melt inside the droplets but only the surface layer. The interior composition is not monitored; bulk melt composition is used instead.
Steel melt mass conservation equation is defined as a sum of the conservation equations of the species in metal.
Slag is modeled as a single volume, the species have only one mass fraction, which is used in the reactions. Conservation equations consist of all reactions involving the species in question. Aluminum oxide conservation is

$$R_1 A_{Al} \nu_{1,Al_2O_3} + R_2 A_f \nu_{2,Al_2O_3} + R_8 A_d \nu_{8,Al_2O_3} = -\frac{d(m_s y_{Al_2O_3})}{dt} \tag{53}$$

SiO_2 FeO and MnO are modelled in a similar way.
The slag mass conservation sums up all the reactions including the slag species.

2.5 Energy conservation

The reaction enthalpies, convection, conduction and radiation are taken into account in the energy conservation system. Calculation is done with the implicit Newton's method, at each timestep after reaction solution loop has converged.
Heat is transferred by radiation between surfaces of the CAS-OB device and its environment. At the outer surfaces, radiation interacts with factory surroundings, which are assumed to be at constant temperature T_{inf}.
At surfaces where radiation from a surface can hit another surface, radiosities J need to be solved. The radiosities of different surfaces affect each other, therefore radiation balance equations were solved implicitly together with other heat transfer conservation equations. Radiation conservation equation for each surface i is[16]

$$\frac{E_{bi} - J_i}{(1-\varepsilon_i)/\varepsilon_i A_i} = \sum_{j=1}^{N} \frac{J_i - J_j}{(A_i F_{ij})^{-1}}. \tag{54}$$

E_{bi} is blackbody radiation, J is radiosity, ε_i is emissivity and F_{ij} is view factor from surface i to surface j.
Most of the view factors were acquired from Ansys Fluent CFD cases, for lowered bell, uplifted bell at normal position and uplifted bell at higher position for pyrometer measurement. The view factors are given in **Table 3** and **4**. The slag open eye size diameter used in the view factor calculations is a constant 0.8 m, which corresponds to the typical argon flow rate.
Radiation heat transfer is simple inside the bell, since there is only three surfaces and two of them are not directly connected by radiation. The radiosities of bell interior (B1), occupied surface (o) and free surface (f) are respectively:

$$J_{B1} = \frac{E_b(T_o)\varepsilon_o F_{B1-o} + E_b(T_f)\varepsilon_f F_{B1-f} + E_b(T_{B1})\frac{\varepsilon_{B1}}{1-\varepsilon_{B1}}}{\varepsilon_o F_{B1-o} + \varepsilon_f F_{B1-f} + \frac{\varepsilon_{B1}}{1-\varepsilon_{B1}}} \tag{55}$$

$$J_o = E_b(T_o)\varepsilon_o + J_{B1}(1-\varepsilon_o) \tag{56}$$

Table 3. View factors when the bell is on melt.

	From surface					
To surface	Free	Occupied	Bell in	Slag	Ladle	Bell exterior
Free			$A_f/A_{B,in}$			
Occupied			$A_o/A_{B,in}$			
Bell in	1.0000	1.0000				
Slag					0.2201	0.1881
Ladle				0.3464	0.0545	0.3230
Bell exterior				0.2195	0.2398	
Environment				0.4341	0.4857	0.4888

Table 4. View factors for uplifted bell cases.

	From surface					
To surface	Open eye	Slag	Ladle	Bell int.	Bell bottom	Bell exterior
Bell at normal position:						
Open eye			0.0069	0.0404	0.0682	
Slag			0.2694	0.1424	0.7289	0.0363
Ladle	0.1073	0.2869	0.0967	0.0297	0.1972	0.1302
Bell in	0.4789	0.1204	0.0255	0.7870		
Bell bottom	0.2009	0.1540	0.0393			
Bell exterior		0.0365	0.1261			
Environment	0.2128	0.4022	0.4361	0.0007	0.0057	0.8334
Bell at pyrometer measurement position:						
Open eye			0.0069	0.0159	0.0488	
Slag			0.2694	0.1081	0.4564	0.0092
Ladle	0.1075	0.2870	0.0970	0.05231	0.2682	0.0374
Bell in	0.1815	0.0894	0.0440	0.7870		
Bell bottom	0.1465	0.0967	0.0529			
Bell exterior		0.0092	0.0356			
Environment	0.5645	0.5176	0.4943	0.0368	0.2265	0.9534

$$J_f = E_b(T_f)\varepsilon_f + J_{B1}(1-\varepsilon_f) \tag{57}$$

View factors in this case are calculated using the reciprocity relation $A_i F_{ij} = A_j F ji$[16]. Since all radiation from surface areas A_f and A_o hit the bell interior, $F_{f-B1} = 1$ and $F_{o-B1} = 1$, and therefore $F_{o-B1} = A_f/A_{B,in}$ and $F_{B1-o} = A_o/A_{B,in}$.

The energy conservation for a massless free surface is described as

$$\begin{aligned}\alpha_l\left(T_l - T_f\right) + \alpha_g\left(T_g - T_f\right) - \left(J_f - J_{B1}\right) \\ + \sum_{k}^{n}\sum_{i=0}^{n_l+n_g} max\left(-R_k\nu_{i,k}, 0\right) C_{p,i}\left(T_{G/L} - T_f\right) = \sum_{k}^{n} R_k \Delta h_k(T_f),\end{aligned} \tag{58}$$

where α is the heat transfer coefficient, α_l in steel and α_g in gas, T is temperature, T_g in gas, T_l in steel, T_f at free surface and T_{B1} on the inner surface of the bell.

Slag and liquid aluminiun inside the bell are assumed to be at the same temperature, and their energy conservation is as follows

$$\begin{aligned}\frac{dm_{Al,l}}{dt} c_{p,Al,l}\left(T_l - T_o\right) + \alpha_{L,o} A_o\left(T_l - T_o\right) + \alpha_{g,o} A_o\left(T_g - T_o\right) - A_o\left(J_o - J_{B1}\right) \\ + \sum_{i=0}^{n_l} R_D y_i c_{p,i}\left(T_l - T_o\right)\eta_D - \sum_{k=7}^{10} R_k A_d \Delta h_k(T_o) + \sum_{i=0}^{n_s}\sum_{k=1}^{7} R_k \nu_{k,i} A_f c_{p,i}\left(T_f - T_o\right) \\ - k_a A_{B1o}(To - T_{B1})/(0.5 d_a) = \left(m_{Al,l} c_{p,Al,l} + m_s c_{p,S}\right)\frac{dT_o}{dt}.\end{aligned} \tag{59}$$

η is heat transfer efficiency defined as $\eta = 1 - exp\left(-\frac{6\alpha_D \tau_D}{d_D c_{p,l}\rho_l}\right)$. Energy conservation of the gas space inside the bell is

$$\begin{aligned}\dot{m}_{O_2,in} c_{p,O_2,in}(T_{O_2,in} - T_g) + \dot{m}_{Ar,in} c_{p,Ar}(T_f - T_g) \\ - R_6 \nu_{6,CO} A_f c_{p,CO}(T_g - T_f) - \alpha_{g,o} A_{Al}(T_g - T_{Al}) \\ - \alpha_g A_f (T_g - T_f) - \alpha_{B,in} A_{B,in}(T_g - T_{B1}) = m_g c_{p,g}\frac{dT_g}{dt}.\end{aligned} \tag{60}$$

The steel melt energy conservation is modelled as

$$\begin{aligned}\dot{m}_{Ar,in} c_{p,Ar}(T_{Ar,in} - T_l) - \frac{m_{Al,s}}{\tau_m}\left(c_{p,Al,s}(T_{melt,Al} - T_{in,Al}) + h_{melt,Al}(T_{melt,Al}) + c_{p,Al,l}(T_{melt,Al})\right) \\ - \alpha_{L,o} A_o\left(T_l - T_o\right) - \alpha_{L,f} A_f\left(T_l - T_f\right) - \alpha_{L,L} A_{L1}\left(T_l - T_{L1}\right) - \alpha_{L.o} S_e\left(T_l - T_{S1}\right) \\ - k_a A_{B1,sub}(T_l - T_{B1})/(0.5 d_a) - k_{brick} A_{B2,sub}\left(T_l - T_{B2}\right)/(0.5 H_{B2}) \\ + \sum_{k=2}^{6}\left(-max(-R_k, 0)\nu_{k,k} A_f c_{p,k}(T_f - T_l)\right) \\ + \sum_{i=0}^{n_l}\left(max\left(R_D y_i + \sum_{k=7}^{10}\left(R_k \nu_{k,i}\right) A_d, 0\right)\right) c_{p,i}(T_o - T_l)\eta_D = m_l c_{p.L}\frac{dT_l}{dt},\end{aligned} \tag{61}$$

where $\alpha_{L,L}$ is the heat transfer coefficient between the ladle wall and the steel melt, and H_{B2} is the height of bell brick layer. Ladle and bell structures are modelled by assuming a one-dimensional temperature gradient normal to the surfaces. The calculation is done in four nodes across the walls, as described in **Figure 5**.

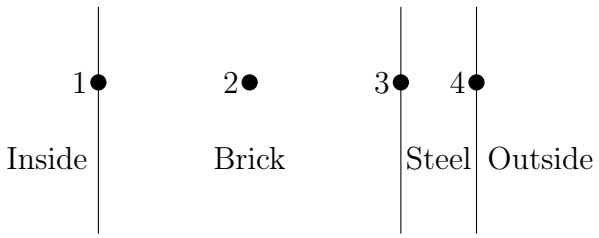

Figure 5. Computational nodes for energy in bell and ladle walls.

Energy conservation equation for ladle inner surface in contact with steel melt, node L_1 is

$$\alpha_{L,L}(T_l - T_{L1}) = k_{brick}(T_{L1} - T_{L2})/(0.5dx_{Lb}), \tag{62}$$

where dx_{Lb} is the ladle brick layer thickness. Equation for node L_2 inside ladle brick layer is

$$k_{brick}A_{L2}(T_{L1} - T_{L2})/(0.5dx_{Lb}) - k_{brick}A_{L2}(T_{L2} - T_{L3})/(0.5dx_{Lb}) \\ - (E_{b,T_{L2}} - J_L)\varepsilon_{brick}A_{L,rad}/(1 - \varepsilon_{brick}) = m_{brick,L}c_{p,brick}\frac{dT_{L1}}{dt}, \tag{63}$$

where A_{L2} is surface area of ladle brick layer and $A_{L,rad}$ is the exposed surface above the melt level.
Energy conservation at the surface in between the ladle brick layer and the steel mantle, node L_3, is

$$k_{brick}A_{L4}(T_{L2} - T_{L3})/(0.5dx_{Lb}) - k_{steel}A_{L4}(T_{L3} - T_{L4})/(0.5dx_{Ls}), \tag{64}$$

where dx_{Ls} is steel shell thickness. Energy conservation equation for node L_4, ladle outer surface, includes a storage term for the steel shell

$$k_{steel}A_{L4}(T_{L3} - T_{L4})/(0.5dx_{Ls}) - \alpha_{L4}A_{L4}(T_{L4} - T_{atm}) \\ - \varepsilon_{steel}A_{L,out}\sigma(T_{L4}^4 - T_{atm}^4) = m_{steel,L}c_{p,steel}\frac{dT_{L4}}{dt}. \tag{65}$$

The bell inner surface energy conservation is

$$\alpha_{B1}A_{B1}(T_g - T_{B1}) + A_o(J_o - J_{B1}) + A_f(J_f - J_{B1}) \\ + k_aA_{B1,sub}(T_l - T_{B1})/(0.5d_a) + k_aA_{B1o}(To - T_{B1})/(0.5d_a) \\ - k_{brick}A_{B1}(T_{B1} - T_{B2})/(0.5dx_{Bb}) - A_{B1}d_a\rho_ac_{p,a}\frac{dT_{B1}}{dt}. \tag{66}$$

Subscript a is for attached material inside the bell surface, thickness d_a is set at 0.01m. Material properties are calculated as a combination of 50% slag and 50% steel.
The energy conservation equations for bell wall nodes 2,3 and 4 are as follows, respectively:

$$k_{brick}A_{B1}(T_{B1} - T_{B2})/(0.5dx_{Bb}) - k_{brick}A_{B2}(T_{B2} - T_{B3})/(0.5dx_{Bb}) \\ + k_{brick}A_{B2,sub}l_{bell}\left(T_l - T_{B2}\right)/(0.5H_{B2}) = m_{brick,B}c_{p,brick}\frac{dT_{B2}}{dt} \tag{67}$$

$$k_{brick}A_{B2}(T_{B2} - T_{B3})/(0.5dx_{Bb}) = k_{steel}A_{B3}(T_{L3} - T_{L4})/(0.5dx_{Bs}) \quad (68)$$

$$k_{steel}A_{B4}(T_{B3} - T_{B4})/dx_{Bs} - \alpha_{B4}A_{B4}(T_{B4} - T_{atm}) - (E_{b,T_{B4}} - J_{B4})\varepsilon_{steel}A_{B4}/(1 - \varepsilon_{steel}) = m_{steel,B}c_{p,steel}\frac{dT_{B4}}{dt} \quad (69)$$

The energy conservation for slag layer outside the bell is modeled with two equations, one for lower surface

$$\alpha_{L,o}(T_l - T_{S1}) = k_s(T_{S1} - T_{S2})/h_{slag} \quad (70)$$

and another for upper surface

$$k_s(T_{S1} - T_{S2})/h_{slag} = (E_{b,T_{S2}} - J_{S2})\varepsilon_{slag}/(1 - \varepsilon_{slag}). \quad (71)$$

2.6 Model for an elevated bell

A cooling model was constructed for a situation where the bell has been lifted above the ladle after the heating period. The cooling rate is needed in order to use the bell cooling data obtained during the first round of measurements. In this part of the simulation, the geometrical parameters are different in the radiation model as the bell is lifted above the ladle.
At this stage of the process, there are no reactions in the model, only cooling of the ladle and bell and their interaction through heat radiation.
Energy conservation equations are otherwise the same as in the main model, except that the radiation situation is different and the reactions are absent.

2.7 Calculation

The implicit Euler method is used in time integration of the conservation equations. Mass conservation system consists of 36 equations, energy system has 17 equations when bell is down and 18 when bell is lifted above the melt. The uplifted case has one more unknown radiosity variable, and therefore one more equation. The energy and mass conservation parts are solved separately, mass part first. Flow chart of the model is presented in **Figure 6**. Newton's method is used with Jacobian matrix consisting derivatives with respect to every variable. In mass conservation system the derivatives are analytical for stability, in energy part numerical differences are used.

2.8 Measurements

The industrial measurements from CAS-OB were carried out at the SSAB steel plant in Raahe, Finland. The first round of measurements were made in January 2014, and the second round in April 2015. By using normal steel plant equipment, steel and slag samples were taken and temperature was measured by probe. The steel samples were analyzed with optical emission spectroscopy (OES) and slag samples with X-ray fluorescence spectroscopy (XRF). In the first

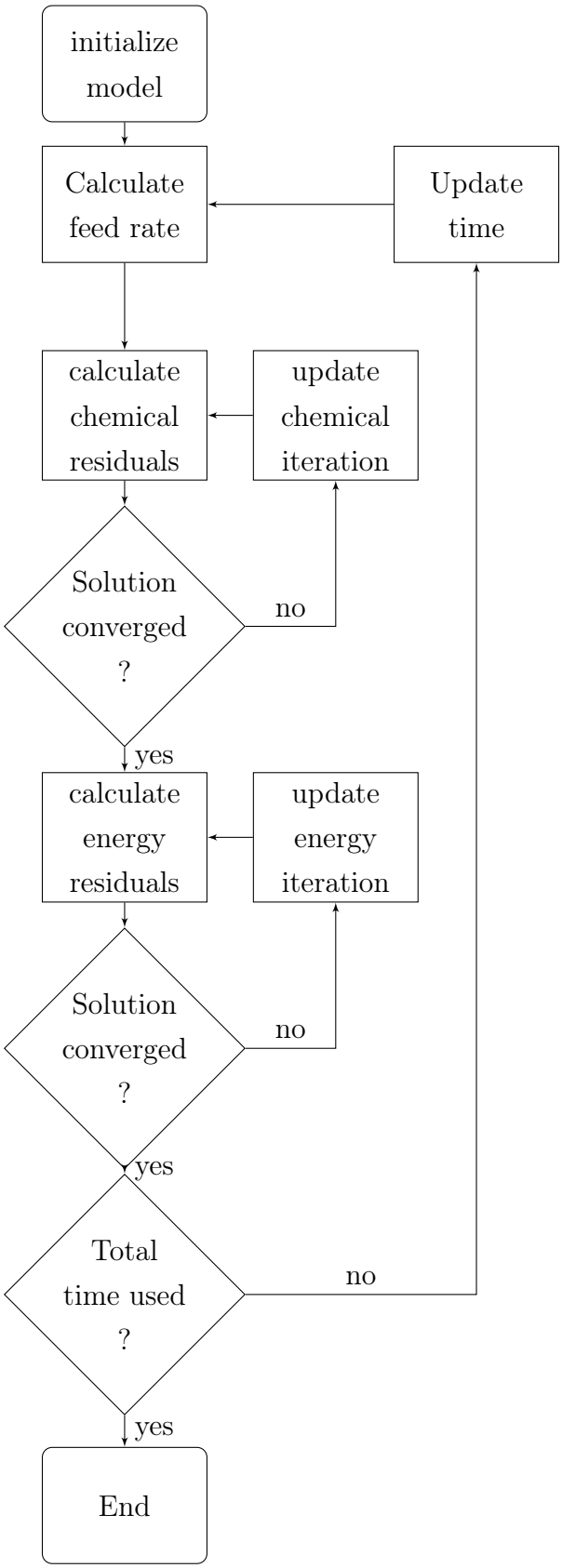

Figure 6. Flow chart of the model

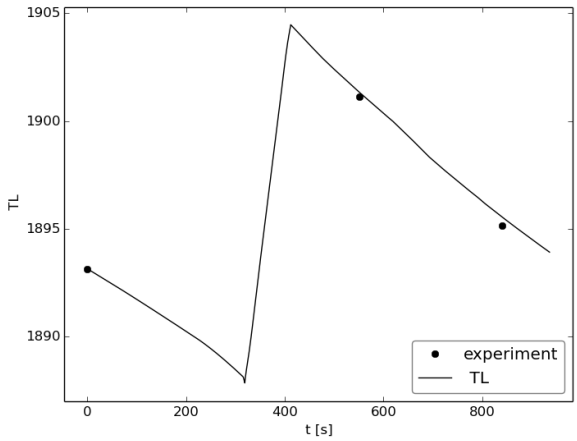

Figure 7. Simulated steel melt temperature with measurement data, heat 2014/2.

campaign temperatures were additionally measured with pyrometer DIAS Pyrospot DSR10N and thermal camera Optris PI120 . The pyrometer provided temperatures from bell inner surface as soon as the bell was lifted above the ladle making the measurement possible. The thermal camera was used to monitor the outer surfaces of the ladle and bell. The first set of measurements unfortunately does not contain steel samples directly after the heating stage, the sample was taken after reduction stage. Temperature measurements were always taken before and after the heating stage. The temperature measurement equipment used is reasonably accurate, temperature probe error is 1 K, pyrometer error is 0.5% and thermal camera error 2%.

3 Results

3.1 Temperature

The most important result of the model is the temperature of the steel melt during heating. Simulations start at temperature measurement before heating, in the beginning, the melt is cooling until heating is started, and after heating the cooling starts again. Typical temperature curve can be seen in **Figure 7**. Simulated and measured temperatures after heating in all studied heats are presented in **Figure 8a**. End temperatures are given in **Figure 8b**. Separate data of first and second measurement campaign are given in **Table 5**. Simulated results are compared to measurement data with mean absolute errors (MAE), given in the tables.

Thermal camera and pyrometer measurement data and corresponding simulation data is presented as individual curves for all the four cases for which measurement data is available. The bell interior temperature starts to rise as the bell is lowered into the melt, and then cools again after heating. Simulation data, with somewhat distorted measurement data, is given in **Figure 9**.

The ladle outer surface temperature is almost constant at 600 K in all cases, and is simulated and measured in **Figure 10**. The inner surface temperature closely follows the steel melt temperature.

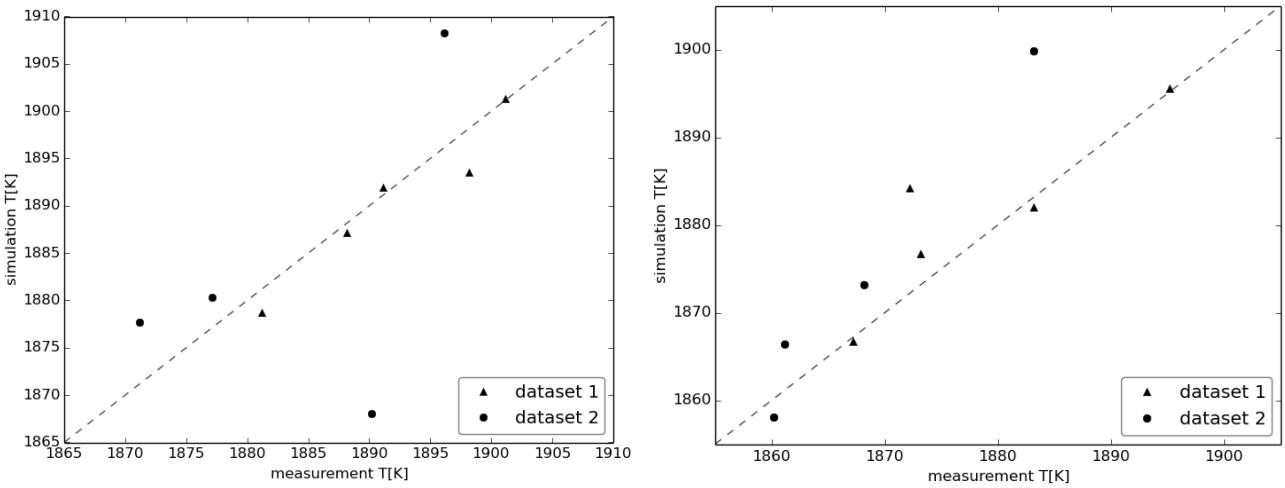

(a) Steel temperature after heating.

(b) Steel end temperature.

Figure 8. Simulation vs. measurement of steel temperature.

Table 5. Temperature measurements and simulation results.

	before T[K]	after T[K]	end T[K]		before T[K]	after T[K]	end T[K]
heat 2014/1				heat 2015/1			
measurement	1870	1881	1867	measurement	1868	1877	1868
simulation		1878.7	1866.8	simulation		1880.3	1873.2
heat 2014/2				heat 2015/2			
measurement	1893	1901	1895	measurement	1869	1871	1861
simulation		1901.3	1895.6	simulation		1877.7	1866.5
heat 2014/3				heat 2015/3			
measurement	1884	1891	1872	measurement	1858	1890	1860
simulation		1891.9	1884.2	simulation		1868.0	1858.1
heat 2014/4				heat 2015/4			
measurement	1876	1888	1873	measurement	1898	1896	1883
simulation		1887.2	1876.7	simulation		1908.3	1899.9
heat 2014/5							
measurement	1886	1898	1883				
simulation		1893.5	1882.0				
MAE		1.8	3.5	MAE		11.0	7.3

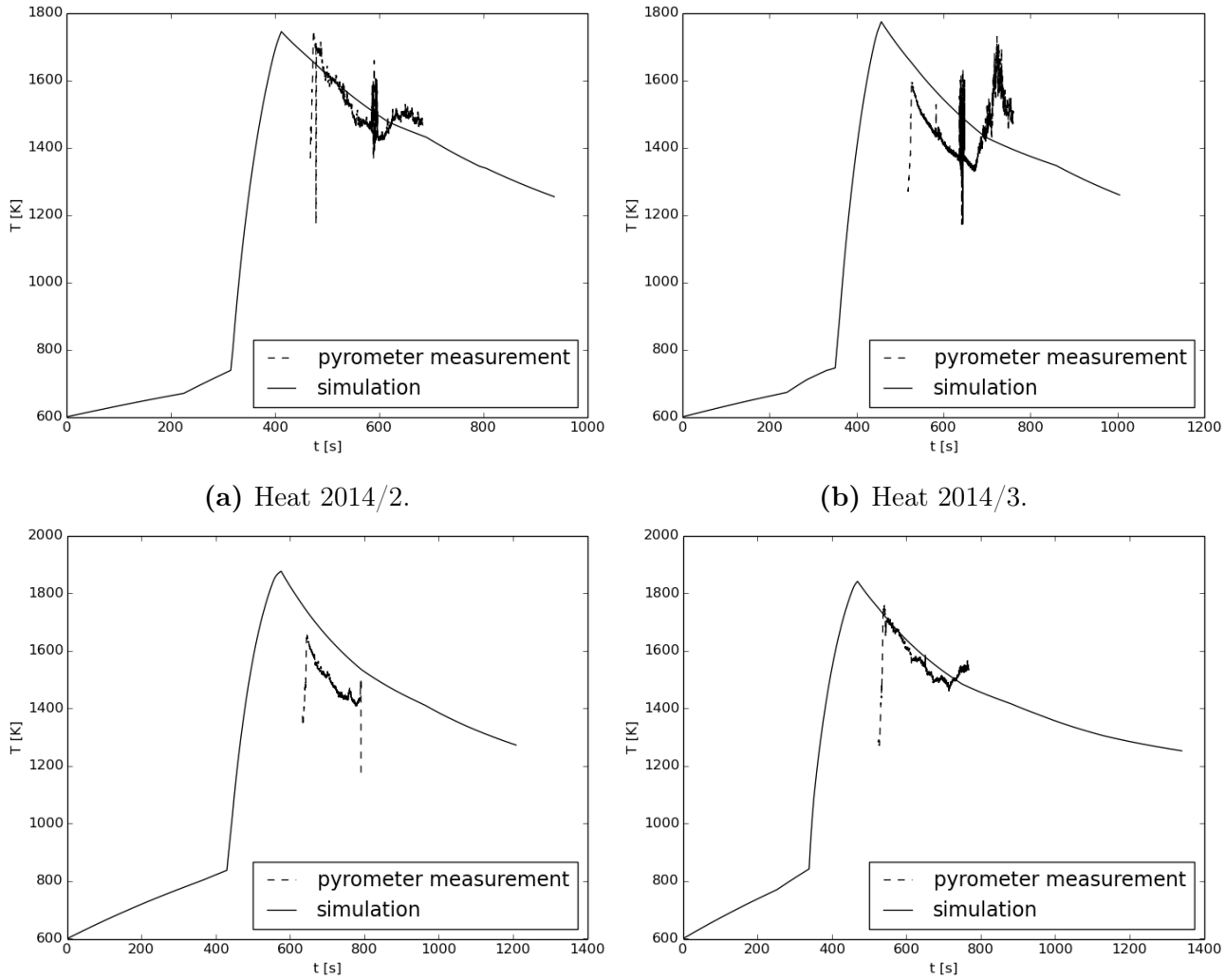

(a) Heat 2014/2.

(b) Heat 2014/3.

(c) Heat 2014/4.

(d) Heat 2014/5.

Figure 9. Bell interior temperature, simulation and pyrometer measurement from elevated bell, in different heats.

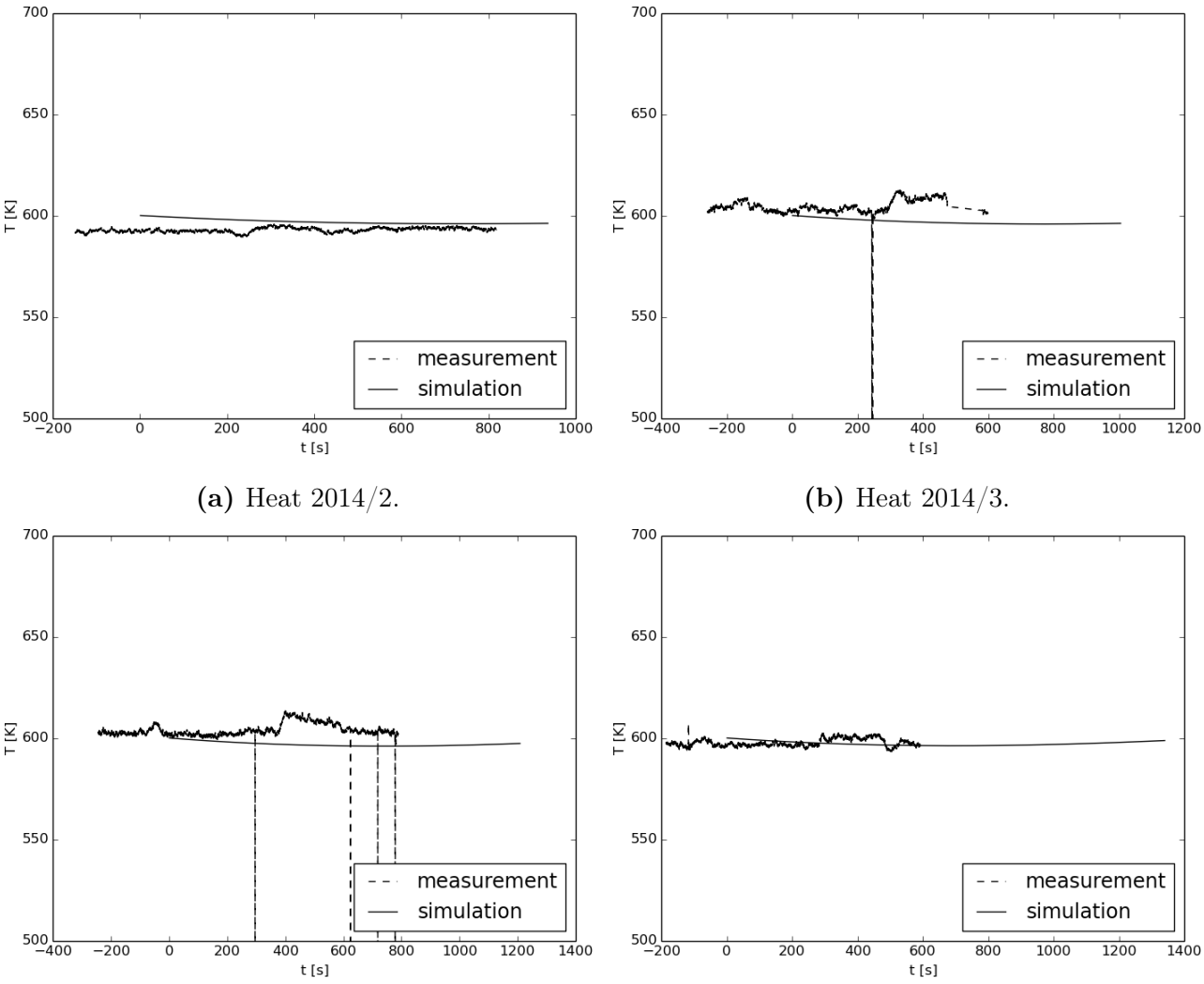

(a) Heat 2014/2.

(b) Heat 2014/3.

(c) Heat 2014/4.

(d) Heat 2014/5.

Figure 10. Ladle exterior temperature, simulation and thermal camera measurement, in four different heats.

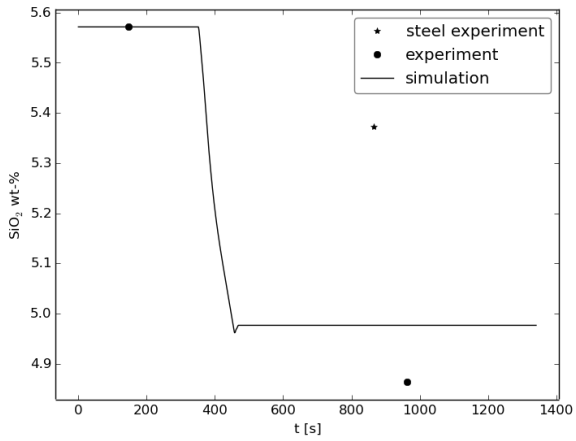

Figure 11. SiO_2 mass fraction in slag, heat 2014/5.

3.2 Chemical composition

The model gives the mass fraction of each element as a function of time, and conservation of mass is fulfilled between phases, element leaving steel melt is found in slag or gas phase. This is not the same in the measurement data: the change in one phase does not always match the change in the other phase. For example, if we use steel melt measurement data of the change in silicon content to calculate corresponding amount of SiO_2 in the slag, the result does not match with measured SiO_2 change. SiO_2 simulation with end measurement data calculated from both phases is presented in **Figure 11**. Steel composition data is presented in **Table 6** and slag data is presented in **Table 7**. For comparison of simulated data with measured data, the corresponding data points of all heats are plotted in **Figure 12** and **13**.

Table 6. Steel measurements and simulation results in wt%.

	C	Si	Mn	Al		C	Si	Mn	Al
heat 2014/1					heat 2015/1				
before	0.034	0.013	0.193	0.034	before	0.05	0.131	1.32	0.031
after	0.034	0.014	0.182	0.036	after	0.05	0.104	1.25	0.04
simulation	0.034	0.010	0.184	0.054	simulation	0.050	0.113	1.263	0.033
heat 2014/2					heat 2015/2				
before	0.05	0.009	0.202	0.05	before	0.051	0.135	1.38	0.045
after	0.051	0.009	0.195	0.045	after	0.054	0.119	1.31	0.057
simulation	0.050	0.007	0.194	0.065	simulation	0.051	0.123	1.338	0.060
heat 2014/3					heat 2015/3				
before	0.039	0.007	0.195	0.029	before	0.103	0.21	0.704	0.043
after	0.039	0.009	0.183	0.047	after	0.098	0.161	0.598	0.059
simulation	0.039	0.005	0.187	0.044		0.102	0.188	0.673	0.051
heat 2014/4					heat 2015/4				
before	0.033	0.011	0.171	0.042	before	0.039	0.008	0.394	0.036
after	0.034	0.011	0.158	0.049	after	0.039	0.007	0.36	0.047
simulation	0.033	0.007	0.160	0.067	simulation	0.039	0.005	0.372	0.057
heat 2014/5									
before	0.031	0.009	0.169	0.043					
after	0.032	0.01	0.159	0.051					
simulation	0.031	0.007	0.161	0.065					
MAE	0.001	0.003	0.002	0.015	MAE	0.002	0.011	0.032	0.007

Table 7. Slag measurements and simulation results in wt%.

	Al_2O_3	SiO_2	MnO	FeO		Al_2O_3	SiO_2	MnO	FeO
heat 2014/1					heat 2015/1				
before	36.816	5.935	1.711	3.337	before	31.733	13.105	1.506	0.914
after	42.160	5.229	2.544	6.055	after	31.409	13.702	7.768	1.483
simulation	39.775	5.543	2.422	8.864	simulation	34.062	13.814	7.741	1.352
heat 2014/2					heat 2015/2				
before	33.942	5.602	1.354	3.632	before	34.692	11.310	1.275	0.522
after	41.225	5.126	2.264	3.508	after	35.129	11.993	7.111	1.511
simulation	38.702	5.052	2.130	7.969	simulation	37.695	11.616	5.499	0.941
heat 2014/3					heat 2015/3				
before	32.320	5.478	1.990	6.089	before	36.384	10.521	1.322	1.034
after	41.207	4.458	3.103	6.112	after	38.223	10.179	7.133	10.710
simulation	36.635	4.871	2.586	11.152	simulation	38.267	12.846	4.486	1.465
heat 2014/4					heat 2015/4				
before	33.813	5.110	1.692	4.154	before	37.924	5.386	3.866	4.457
after	43.560	4.529	2.518	4.217	after	43.681	4.626	6.668	5.110
simulation	39.071	4.690	2.603	10.771	simulation	41.375	4.807	5.329	9.104
heat 2014/5									
before	30.917	5.572	1.559	5.144					
after	39.777	4.864	2.243	4.366					
simulation	37.572	4.976	2.251	9.124					
MAE	3.235	0.215	0.173	4.724	MAE	1.892	0.834	1.406	3.485

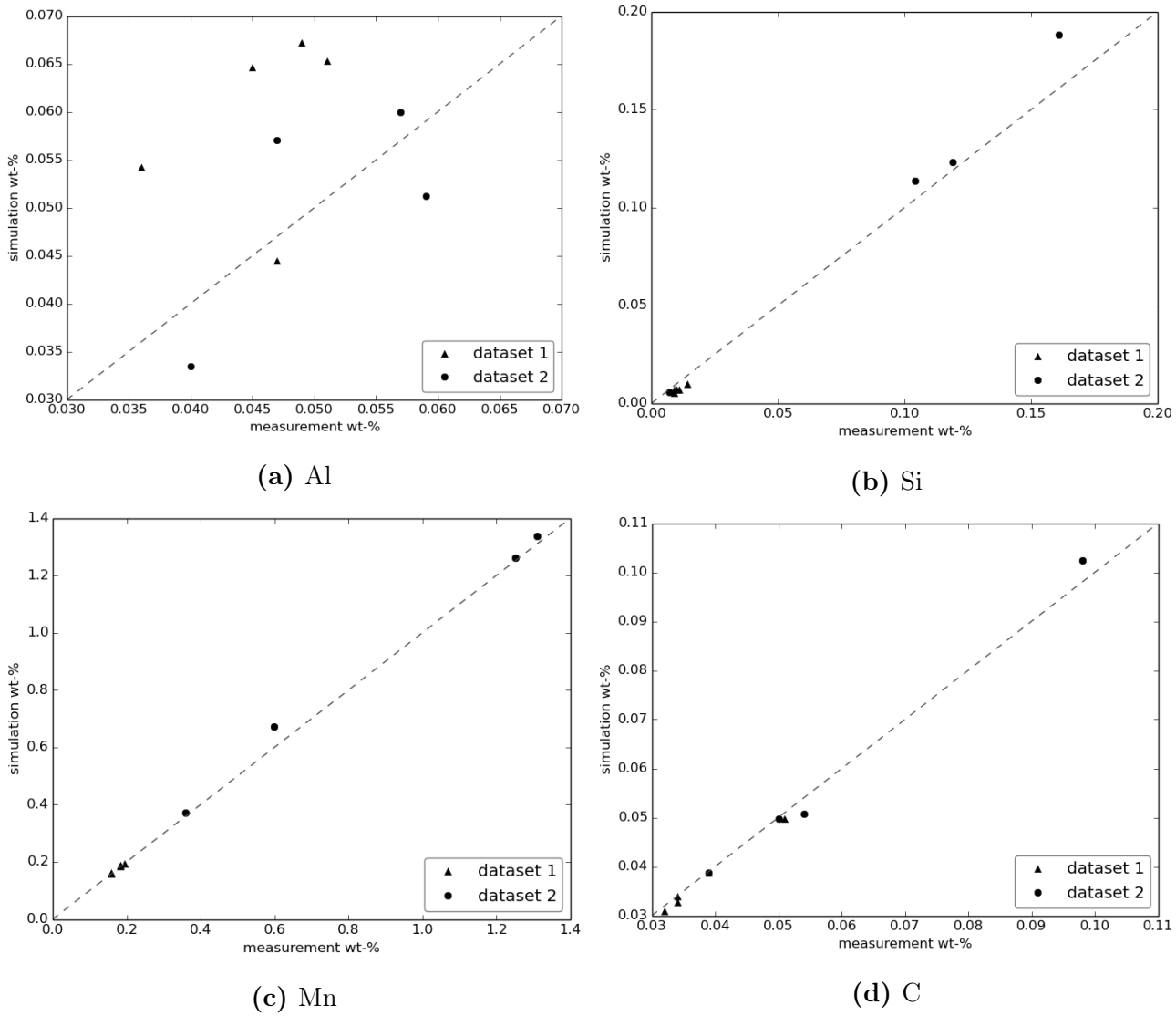

(a) Al

(b) Si

(c) Mn

(d) C

Figure 12. Simulation vs. measurement of species in steel.

4 Discussion

Pyrometer and thermal camera measurement data show some fluctuations that differ from simulation results. The sharp peaks in the pyrometer measurement curves occur when samples are taken from the melt, causing flames and smoke. The rise in the temperature in the end of the curves is caused by increased argon bottom blowing, which brings hot gas and dust into the bell.

The simulated temperature results match very well with the measurements of the first dataset, but not with those of the second dataset. The major difference in the data is that steel in three of four heats of the second dataset is Al-Si-killed, whereas the steel in fourth heat is Al-killed, as is the steel in all five heats in the first data set. Perhaps the main reason for the error is the effect of the ladle temperature in the beginning. In the simulations, the initial temperature profile of the ladle is always the same, but this is not the case in the steel plant operation. The ladles are waiting empty for different lengths of time before tapping and CAS-OB treatment. At heat 2015/5 (**Table 5**), the steel cools during heating according to measurements. It was

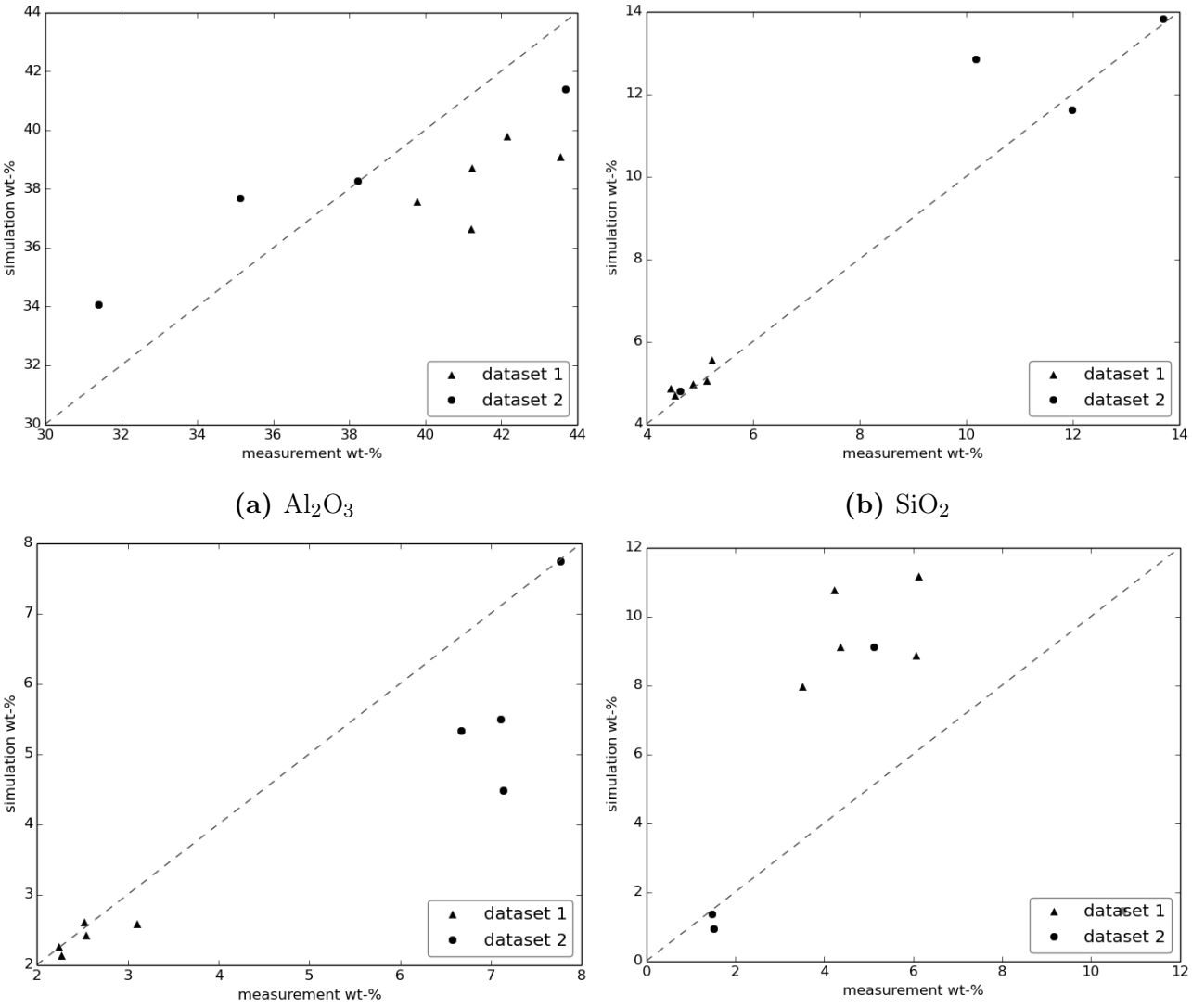

(a) Al_2O_3 **(b)** SiO_2

(c) MnO **(d)** FeO

Figure 13. Simulation vs. measurement of slag components.

found that the ladle had been empty 461 minutes before tapping, whereas the average time is about 100 minutes. In the future, an additional cooling model is needed for an empty ladle, in order to correctly set the initial temperature of the ladle. Some inaccuracy might result from inhomogeneity of the melt, in some heats the melt is mixed with strong argon bubbling before the temperature measurement, and in some others not. Clearly erroneuos measurements are after heating temperature of heat 2015/3 and end temperature of heat 2014/3.
The predicted steel bath compositions generally match the measurements well, but sometimes poorly. From the data, it can be seen that sometimes predicted mass fraction is further away from the end result than initial value. This is partly due to the error in the measurements and small changes of concentrations during the studied process. In general, in the simulation results there is too much FeO in the slag and not enough Al_2O_3 and MnO. Other results match the measurements quite well considering the uncertainty in the measurements. The end composition measurements were taken after the slag reduction stage in the first dataset, which partly explains the error in the slag. In the future the heating stage model can be combined with a reduction stage model developed by Sulasalmi et al.[27]. The resulting model could be used to predict the whole CAS-OB process.

5 Conclusions

The aim of this study was to improve and validate a model we proposed earlier[7]. The CAS-OB heating stage model has been extensively updated and validated with industrial measurements. CFD modeling has been successfully used to determine heat and mass transfer coefficients. The reaction model has been updated to fulfill chemical equilibrium at the reaction surfaces. The heat transfer model has been extended to include the bell also in upper position, and radiation heat transfer for all radiating surfaces. Industrial measurements of temperature and chemical composition show that the model is functioning correctly. The model can be used to predict temperature, as long as the initial values are known. To accurately predict chemical species, further validation and new, more accurate measurements are needed. In its current state the model can be used in process development. Process control usage will be possible in the future, when further precision is added to the model.

Acknowledgements

For funding this work, we would like to acknowledge Business Finland (DIMECC SIMP project), Academy of Finland (projects 258319 and 26495), The Jenny and Antti Wihuri Foudation, Tauno Tönning Foudation and Finnish Culture Foundation. We would like to thank SSAB for cooperation.

References

[1] G. Stolte, *Secondary Metallurgy*, Verlag Stahleisen, Düsseldorf, Germany **2007**.

[2] L. Nilsson, K. Andersson, K. Lindquist, *Scand. J. Metall.* **1996**, *25*, 73.

[3] L. Jonsson, C.E. Grip, A. Johansson, P. Jönsson, *Steelmaking Conf. Proc.* **1997**, *80*, 69.

[4] T. Kulju, S. Ollila, R.L. Keiski, E. Muurinen, *Mater. Sci. Forum* **2013**, *762*, 248.

[5] W.J. Ma, Y.P. Bao, L.H. Zhao, M. Wang, *Ironmak. Steelmak.* **2014**, *41*, 607.

[6] Y. Pan, D. Guo, J. Ma, W. Wang, F. Tang, C. Li, *ISIJ Int.* **1994**, *34*, 794.

[7] M. Järvinen, A. Kärnä, V.-V. Visuri, P. Sulasalmi, E.P. Heikkinen, K. Pääskylä, C. De Blasio, S. Ollila, T. Fabritius, *ISIJ int.* **2014**, *54*, 2263.

[8] M. Järvinen, A. Kärnä, T. Fabritius, *Steel Res. Int.* **2009**, *80*, 429.

[9] A. Kärnä, M. Järvinen, T. Fabritius, *Steel Res. Int.***2015**, *86*, 1370.

[10] J. Szekely, G. Carlsson, L. Helle, *Ladle Metallurgy*, Springer-Verlag, New York, USA **1989**.

[11] Y. Xu, M. Ersson, P. Jönsson, *Metall. Mater. Trans. B* **2015**, *46*, 2628.

[12] H. Kataoka, T. Miyauchi, *Chem. Eng.* **1969**, *33*, 181.

[13] M. Laakkonen, V. Alopaeus, J. Aittamaa, *Chem. Eng. Sci.* **2006**, *61*, 218.

[14] G. Venturini, M.B. Goldschmit, *Metall. Mater. Trans. B* **2007**, *38*, 461.

[15] Y. Kawai, Y. Shiraishi, *Handbook of Physico- chemical Properties at High Temperatures*, Iron and Steel Institute of Japan **1988**.

[16] F.P. Incropera, D.P. De Witt, *Fundamentals of Heat and Mass Transfer*, John Wiley & Sons, New York, USA **1985**.

[17] G. Ebneth, W. Pluschkell, *Steel Res. Int.* **1985**, *56*, 513.

[18] K. Krishnapisharody, G.A. Irons, *ISIJ Int.* **2008**, *48*, 1807.

[19] R. Higbie, *Trans. Am. Inst. Chem. Eng.* **1935**, *31*, 365.

[20] S.C. Koria, K.W. Lange, *Steel Res. Int.* **1987**, *58*, 421.

[21] B.K. Rout, G. Brooks, Subagyo, M.A. Rhamdhani, Z. Li, *Metall. Mater. Trans. B* **2016**, *47*, 3350.

[22] Subagyo, G.A. Brooks, K.S. Coley, G.A. Irons, *ISIJ Int.* **2003**, *43*, 983.

[23] G. Brooks, Y. Pan, Subagyo, K. Coley, *Metall. Mater. Trans. B* **2005**, *36*, 525.

[24] P. Linstrom, E.W.G. Mallard (eds.), *NIST Chemistry WebBook.*, NIST Standard Reference Database Number 69, National Institute of Standards and Technology **2017**.

[25] Outotec, *HSC Chemistry 8* **2015**.

[26] V.V. Visuri, M. Järvinen, A. Kärnä, P. Sulasalmi, E.P. Heikkinen, P. Kupari, T. Fabritius, *Metall. Mater. Trans. B* **2017**, *48*, 1850.

[27] P. Sulasalmi, V.V. Visuri, A. Kärnä, M. Järvinen, S. Ollila, T. Fabritius, *Metall. Mater. Trans. B* **2016**. *47*, 3544.

A numerical model for the heating stage of the CAS-OB process is presented. The model utilizes results from CFD simulations in a process model written in c++. Chemical reactions and energy conservation are calculated as a function of time.

Aki Kärnä*, Mika Järvinen, Petri Sulasalmi, Ville-Valtteri Visuri, Seppo Ollila and Timo Fabritius

An Improved Model for the Heat-up Stage of the CAS-OB Process: Development and Validation